Large Scale Simulation of Normal Grain Growth via Diffusion Generated Motion

Matt Elsey*, Selim Esedoḡlu, and Peter Smereka
Department of Mathematics, University of Michigan, Ann Arbor, MI 48109, USA

July 26, 2010

Abstract

Diffusion generated motion is used to perform a very large scale simulation of normal grain growth in three dimensions with high accuracy. The method is based on the diffusion of signed distance functions and shares similarities with level set methods. The Herring angle condition at junctions and topological transitions are naturally captured with this formulation. This approach offers significant advantages over existing numerical methods and allows for accurate computations on scales not previously possible. A fully-resolved simulation of normal grain growth initially containing over 130,000 grains in three dimensions is presented and analyzed. It is shown that the average grain radius grows as the square root of time and the grain size distribution is self-similar. Good agreement with other theoretical predictions, experimental results, and simulation results via other techniques is also demonstrated.

Keywords: grain growth; grain boundary; microstructure; simulation; level set.

1 Introduction

Grain growth is an important process by which the microstructure of a polycrystalline material (including most metals and ceramics) evolves during manufacturing processes. Statistical measures of the resultant microstructure affect important macroscale properties of the material, such as its conductivity and brittleness. Manufacturing processes must typically be tuned to provide for an optimal blend of desired material properties; however, performing such tuning experimentally is costly and time consuming. As a result, simulations of grain growth have been attempted using a variety of numerical techniques. Several common techniques are described in Section 3.

Grain growth occurs when polycrystalline materials are annealed. The well-known model for grain growth [3, 15, 31] gives the normal velocity (outward from phase Σ_k) of the interface $\Gamma_{k\ell}$ by

$$v_n(\Gamma_{k\ell}) = \mu\gamma_{k\ell}\kappa_{k\ell}, \tag{1}$$

Here, μ denotes the boundary mobility, $\gamma_{k\ell}$ the grain boundary energy per unit area for the interface $\Gamma_{k\ell}$, and $\kappa_{k\ell}$ the mean curvature of the boundary separating two grains. We use the convention that if phase Σ_k is a spherical grain of radius r surrounded by phase Σ_ℓ, $\kappa_{k\ell} = -2/r$.

We specialize to the case where all surface tensions are constant and equal: $\gamma = \gamma_{k\ell}$, often called "isotropic grain growth." We aim to extend to the more general case given by Equation 1 in future work. The theory for this extension is complete in two dimensions in the absence of topological events. Additional study of topological events such as the division of four junctions following grain disappearence is still required. Here, we nondimensionalize the normal velocity using the mean initial grain radius $\langle r_0 \rangle$, derived from the

*Corresponding author. Email: melsey@umich.edu

mean initial grain volume $\langle V_0 \rangle$ by $\langle r_0 \rangle = (3\langle V_0 \rangle/(4\pi))^{1/3}$. We define the nondimensionalized curvature as $\kappa^\star_{k\ell} = \langle r_0 \rangle \kappa_{k\ell}$. We further nondimensionalize the velocity as $v_n(\Gamma_{k\ell}) = V \cdot v^\star_n(\Gamma_{k\ell})$, with velocity $V = \langle r_0 \rangle / T$ and time $T = \langle r_0 \rangle^2/(\mu\gamma)$, so that

$$v^\star_n(\Gamma_{k\ell}) = \kappa^\star_{k\ell}. \tag{2}$$

As shown in [33] and [52], this nondimsionalized normal speed arises as gradient descent for the nondimensional energy

$$E^\star = \sum_{k<\ell} (\text{area of } \Gamma_{k\ell}). \tag{3}$$

We note that the time scale T is chosen so that $t^\star = 1/4$ is the time required for an isolated grain of radius $\langle r_0 \rangle$ to disappear under pure curvature motion in the nondimensional system. Herafter, we drop the $\star$ notation and refer solely to the nondimensionalized quantities, e.g. the nondimensionalized energy $E^\star$ will be referred to as E.

The algorithm used in this work is fully described in [7]. For the convenience of the reader, we briefly discuss it in Section 2. In this work, we present a large-scale three-dimensional simulation of grain growth, far beyond the scale of simulations presented previously. This simulation is performed on a parallelized version of the code executing on a large cluster. The results are analyzed in great detail and compared to numerous theoretical predictions, results from experiments and smaller simulations performed with various numerical methods. The initial condition contains over $130,000$ fully resolved grains and the evolution is simulated until only about $14,000$ remain. We present various statistics collected throughout this simulation. In particular, we demonstrate the anticipated self-similar character of the grain size distribution as it evolves in time. Furthermore, our results show good agreement with other three-dimensional predictions for grain growth, such as power law growth of the mean grain volume, and three-dimensional version of the Aboav–Weaire law [1, 45] and the Mullins extension of the two-dimensional von Neumann–Mullins relationship [32].

2 Algorithm

Our algorithm is an extension of *distance function-based diffusion generated motion* [8], which is in turn a variant of the *threshold dynamics* scheme proposed by Merriman, Bence, and Osher [30]. The threshold dynamics scheme reduces the computation of various geometric motions of an interface to the alternation of two highly efficient operations: convolution of a characteristic function representing the interior of the interface with a circularly symmetric kernel, and thresholding the convolution output to return to a characteristic function. On a uniform grid with n grid points, the complexity of these operations is just $O(n \log n)$ per time step. The method is also unconditionally stable, so that the only restrictions on the size of the time step are due to accuracy considerations. A major drawback of the threshold dynamics algorithm is that it is very inaccurate on uniform grids, because the interface must be represented as the boundary of a characteristic function, disallowing any possibility of sub-grid accuracy in the absence of adaptive grid refinement (as is explored in [38]).

A signed distance function-based algorithm for diffusion generated geometric motions of the same types attainable by threshold dynamics is proposed in [8]. This algorithm is a modification of the threshold dynamics algorithm, replacing the characteristic function of the set used in threshold dynamics with a signed distance function to the boundary of the set, and the thresholding operation by a redistancing operation. The redistancing operation reconstructs the signed distance function to the boundary of the set from the convolution output, much as the thresholding operation reconstructs the characteristic function of the set from convolution output in threshold dynamics.

Unlike the characteristic function of a set, the signed distance function is a Lipschitz continuous function. This allows for sub-grid accuracy in locating the interface on a uniform grid. Furthermore, fast algorithms are known for constructing signed distance functions (e.g. [36, 51]), so that the computational complexity of the signed-distance function based algorithm is still $O(n \log n)$ per time step. A more detailed discussion of the differences between [30] and [8] can be found in [8].

The threshold dynamics scheme was extended by Ruuth [37] to multiphase motion by mean curvature, the case occurring in grain growth, but the same accuracy limitations faced by the original threshold dynamics scheme still apply. Standard level set techniques have also been applied to the grain growth problem in [52, 9]. The level set method is a sharp interface method, similar to the signed distance function technique we use here (which may itself be considered a special type of level set method). Standard level set methods place only very loose restrictions on the details of the level sets used to implicitly represent the interface. For example, the size of the gradient $|\nabla\phi|$ of the level set function ϕ is generally restricted from becoming too large or too small. This restriction is insufficient for multiphase motion, as first noted and fully explained in [8]. The standard boundary condition for grain growth is the Herring angle condition, described in [16]. For equal surface tensions, the condition states that triple junctions must meet at angles of 120°. In level set methods, an $O(1)$ error is in general introduced in the motion of triple junctions due to differences in the profiles of the level sets representing the three phases. This error also prevents the correct angle conditions from being obtained.

In contrast, [8] provides analytical justification and extensive numerical convergence studies showing that the correct behavior is obtained at junctions under the multiphase version of the signed distance function-based algorithm for motion by mean curvature introduced there. The algorithm for multiphase motion is given in [8], with an enhancement allowing for the simulation of N grains using only $M \ll N$ signed distance functions described fully in [7]. This is achieved by representing large collections of individual, well-separated grains with a single signed distance function. Easily implemented precautions are taken to prevent non-physical interactions from occurring between grains contained in a single signed distance function.

The signed distance function-based algorithm for multiphase motion by mean curvature described in [7] and applied in this work can be thought of as a particular type of level set method. In order to obtain the correct behavior at triple junctions, there is a stronger restriction on the level sets than ordinarily enforced; however, other hallmarks of the level set method are retained: the interfaces are implicitly represented (the algorithm operates only on the values of the signed distance function at grid points), sub-grid accuracy is obtained due to the Lipschitz continuity of the level sets, and the interface is sharp (unlike phase field methods, in which the interface is represented by a diffuse transition layer). On the other hand, standard level set methods for evolution by mean curvature require the solution of a degenerate, highly nonlinear partial differential equation. In contrast, the present algorithm is unconditionally stable (allowing much larger time steps to be taken), a feature inherited from its close connection to the diffusion generated motion of threshold dynamics.

The initial condition is taken to be the Voronoi diagram for N_0 seeds placed uniformly at random in the computational domain D. The N_0 initial grains are contained in sets Σ_i, $i = 1, \ldots, N_0$, with $\cup_i \Sigma_i = D$ and $\cap_i \Sigma_i = \emptyset$. We partition the sets Σ_i into $M \ll N_0$ disjoint sets Ξ_k, such that $\cup_{i=1}^{N_0} \Sigma_i = \cup_{k=1}^{M} \Xi_k$. We maintain M signed distance functions $d_k(x)$, giving the signed distance to the set Ξ_k, with $d_k(x) > 0$ for $x \in \Xi_k$. For example, in the grain growth simulation described in Section 4 we have $N_0 = 133,110$ and $M = 64$. The signed distance functions are updated using the following algorithm:

For $j = 0, \ldots, j_{\max}$, perform steps 1–4.

1. Compute $A_k(x) := K_{\Delta t} * d_k^j$ for $k = 1, \ldots, M$, where

$$K_{\Delta t} = G_{\Delta t} \text{ or } K_{\Delta t} = \frac{1}{4}\left(4G_{\frac{3}{2}\Delta t} - G_{3\Delta t}\right) \text{ with } G_{\Delta t} = \frac{1}{4\pi\Delta t} e^{-\frac{|x|^2}{4\Delta t}}.$$

2. Construct $B_k(x)$ for $k = 1, \ldots, M$ to remove overlaps and vacuums from the previous step:

$$B_k(x) = \frac{1}{2}\left(A_k(x) - \max_{\ell}\{A_\ell(x) : \ell \neq k\}\right)$$

3. Construct the signed distance function $d_k^{j+\frac{1}{2}}(x)$ for $k = 1, \ldots, M$ according to

$$d_k^{j+\frac{1}{2}} = \textbf{Redist}\left(B_k(x)\right).$$

4. If necessary, swap appropriate grains between signed distance functions to ensure that all the grains associated to given signed distance function remain well separated. Denote the resulting signed distance functions as d_k^{j+1}.

For a full description of the algorithm, the reader is referred to [7]. We use a simple cubic lattice with periodic boundary conditions to avoid introducing boundary effects into the evolution except in the case that a single grain grows so large as to be adjacent to itself across a periodic boundary. Such a case cannot arise in normal grain growth until only very few grains remain (e.g. $N(t) \ll 1,000$), which does not occur in the results reported here.

The computational complexity of our algorithm is formally $O(nM \log n)$, where M is the number of level set functions used, and n is the total number of grid points in each set. For a single signed distance function, both the convolution step and the redistancing operation are $O(n \log n)$. The algorithm is second-order accurate in space and first-order accurate in time away from triple points. At triple points, analysis and experiment in [8] suggest that the error is $O(\sqrt{\Delta t})$.

3 Previous Work

A number of other numerical methods have been used to simulate grain growth in previous work. One of the best-known techniques is the Monte Carlo Potts model, implemented in [2]. This model approximates curvature motion by a stochastic series of near-interface cell flipping steps. While the basic Monte Carlo method is quite easy to implement, it is extremely slow and lacks sub-grid accuracy. Furthermore, the stochastic nature of the Monte Carlo evolution ensures that some type of averaging is needed to approximate the true continuum motion. For example, the evolution of a simple circle by mean curvature is very difficult to capture accurately using Monte Carlo methods even on a well-resolved grid. Beyond these significant accuracy concerns, it is also difficult to connect the Monte Carlo method with some notion of "real" time beyond reorientation attempts.

Front-tracking techniques have also been used to simulate mean curvature motion in both two [20, 23] and three [43, 23] dimensions. A major advantage of these techniques is computational efficiency, as computational resources are all devoted to the interface region. The fundamental difficultly inherent to this approach is managing the topological changes that abound in grain growth. With explicit representations of the interface, it is difficult to check if curves (in two dimensions) or surfaces (in three dimensions) intersect. In the case of two-dimensional mean curvature multiphase motion, it is expected (though not fully proven, see [28]) that interfaces interact only through junction–junction collisions. If this conjecture is true, explicitly checking for and handling topological changes may be manageable in this case. However, *no such condition*

is expected to hold in three dimensions. Pinch-off can occur with only two phases in three-dimensional mean curvature motion, as in the standard "dumbbell" example. Topological changes of this type are difficult to detect and manage using front tracking techniques, especially in three dimensions. In contrast, our algorithm handles topological changes naturally, without any additional computation.

The phase field technique has also been used extensively in simulations of grain growth [10, 13, 24, 22, 42] and is much more similar to our algorithm than Monte Carlo or front-tracking techniques. In the phase field method, interfaces are implicitly represented. However, there must be a wide transition region representing the interface between grains. For example, Kim, et al. [22] report that at least six grid points are needed in the transition layer to achieve acceptable accuracy. Therefore, a grain needs to be on the order of at least 25 grid points across to be moderately resolved. In contrast, we demonstrate in [7] that we can simulate evolutions quite accurately with grains approximately ten grid points in each direction, and that we can track them down to half that length with only a few percent relative error. Though there is no rigorous notion of generalized solutions with uniqueness through topological changes, we also perform a convergence study in [7] showing that our simulations track grains through topological changes quite consistently as well. The large grain size requirement imposed by the phase field model is a serious impediment to performing very large-scale simulations.

Our algorithm has all the major advantages of these various computational approaches. It is closely related to both threshold dynamics and level set methods. From threshold dynamics, we inherit unconditional stability, allowing the choice of time step to be restricted only by accuracy considerations. From level set methods, we inherit sub-grid accuracy and graceful handling of topological changes, free from user input. As with front tracking models, we concentrate most of our computational resources at the interface, as the signed distance function computation (the most computationally intensive part of the algorithm) must be performed accurately only in a tubular neighborhood of the interface (with width proportional to $\sqrt{\Delta t}$). As a discretization of Mullins' PDE-based continuum description of grain boundary motion, our algorithm does not suffer from the difficulty of identifying physical time that plagues Monte Carlo-type models.

4 Normal Grain Growth

In this section, a large-scale simulation normal grain growth is described and a wide variety of statistical measures on the resulting microstructure are reported. The simulation begins with 133,110 grains in the domain $D = [0, 82.306]^3$ with periodic boundary conditions. The evolution runs for time $t = 6.2021$, allowing for over 90% of the initial grains to disappear. D is discretized as a regular cubic lattice of size $512 \times 512 \times 512$, and three hundred time steps are taken, ensuring adequate spatial and temporal resolution. The coarsening rate is shown to agree well with theoretical predictions. The grain size distribution is calculated, and exhibits self-similarity. This distribution is compared with a number of different predictions from the literature. In addition, average numbers of grain edges, faces, and corners are computed and compared with other computational approaches and experimental data.

4.1 Qualitative microstructure

We present a three-dimensional simulation with an initial condition containing 133,110 grains. The initial condition was generated as described in Section 2. Figure 1(a) shows a single grain of average size taken from the simulation at $t = 6.2021$. At this time, $\langle r \rangle = 2.11$ and $\langle V \rangle = 39.40$, indicating that mean grain radius has more than doubled the initial value and the mean grain volume is over 9 times the initial mean grain volume. The grain appears to be very well resolved. Its faces, edges, and corners are easy to see. The faces are smooth, and most appear to be concave. Thus this particular grain, which is of average size at this stage in the evolution, must be growing due to the curvature of its interfaces. Overall, the grain resembles what is observed in real materials, such as the beta brass grain shown in Figure 1(b).

The coarsening of the grain pattern is demonstrated by Figure 2. Here we display the grains intersecting the $x = 0$, $y = 0$ and $z = 82.306$ surfaces in the initial condition (a) and after 300 iterations (b). Different colours correspond to different grains. By volume, the average grain at the end of the simulation is nearly

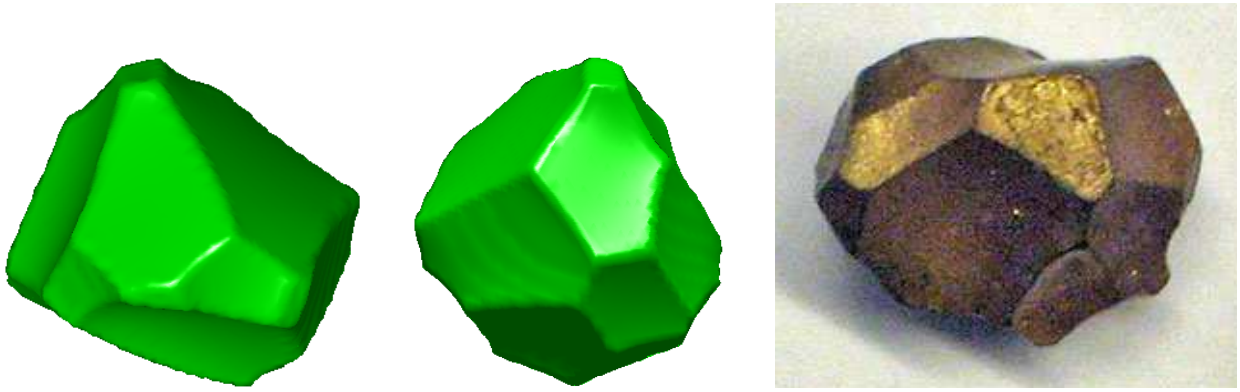

(a) (b)

Figure 1: (a) Two views of a single grain (corresponding to a 180° rotation in the xy-plane) chosen from the evolution after 300 iterations. This grain has nondimensional size $\langle r \rangle = 2.11$, equal to the average grain size at this point in the evolution. The grain is very well resolved, with faces, edges, and corners all easily distinguished. (b) A single grain of beta brass, approximately 2 cm in diameter, from the collection of W.W. Mullins. The photograph is due to K. Barmak and D. Kinderlehrer. The grain compares well to the simulated grain shown in (a).

ten times as large as the average grain at initial condition. In Figure 3 we show all the grains from five of the sixty-four total set functions Ξ at $t = 2.0674$ and $t = 6.2021$. There is a great variability in the size of grains seen in this figure, from grains contained within a single grid cell (equivalent radius $r \approx 0.08$) which are about to disappear, to grains with radius $r \approx 4$.

Cross-sections of successive slices at $t = 6.2021$ are shown in Figure 4(a). Compare to Figure 4(b), showing results from a fully two-dimensional simulation, in which all three junctions must have 120° angles. The cross-sectional views also feature more grains that are long in one dimension and short in the other as compared to the two-dimensional simulation results, where grains tend to be more regularly shaped.

4.2 Energetics

It is shown in [23] that, at least in the absence of topological changes, the surface energy E given by (3) decreases in time under mean curvature motion subject to the Herring angle condition at junctions. It is natural to expect that E would continue to decrease even through topological changes (critical events). We verified that our numerical scheme respects this fundamental behavior by evaluating the energy at every time step. We note that the energy E can be written in terms of the signed distance functions $d_k(x)$ and the Dirac delta function, $\delta(x)$, as the following sum of integrals over the computational domain D:

$$E = \frac{1}{2} \sum_{k=1}^{M} \int_D \delta(d_k(x)) dx. \tag{4}$$

The factor of $\frac{1}{2}$ arises as this formula counts each interface twice. We discretize E as

$$E = \frac{\Delta x^2}{2} \sum_k \sum_{i,j,\ell} \tilde{\delta}(d_k(x_i, y_j, z_\ell)). \tag{5}$$

We utilize a first-order discretization of the delta function, $\tilde{\delta}$, following [39]. The energy E is measured at each time step and is found to decrease monotonically at every time step (see Figure 5(a)) even as the evolution

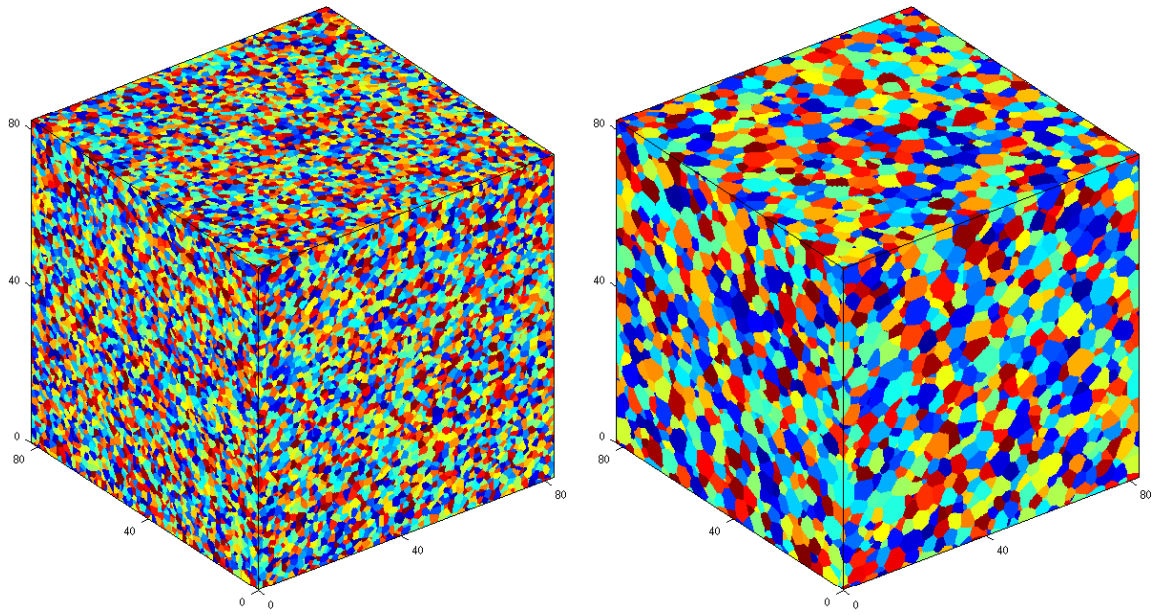

(a) (b)

Figure 2: Visualization of the grain pattern (a) at initial condition and (b) after 300 iterations. The initial condition contains 133,110 grains. At $t = 6.2021$, 14,150 grains remain.

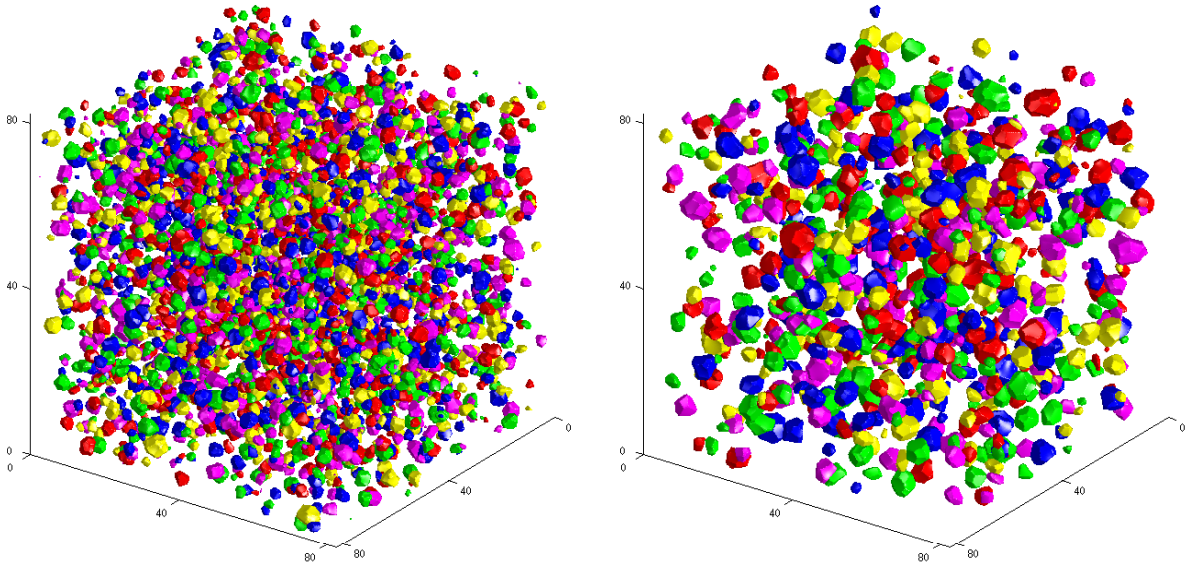

(a) (b)

Figure 3: Grains from five of sixty-four level set functions in the simulation with initially 133,110 grains, after (a) $t = 2.0674$ and (b) $t = 6.2021$. There are 54,197 and 14,150 total grains (in all sixty-four sets), respectively. Only a subset of grains is shown, as otherwise the entire volume would be filled.

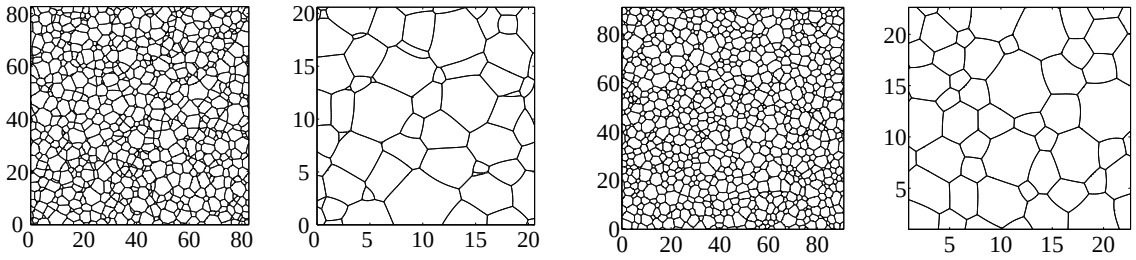

(a) (b)

Figure 4: (a) A cross-sectional slice taken from simulation at $t = 6.2021$. The full slice is shown at left and zoomed in on at right. The curved nature of the interfaces is easily seen. The angles observed at triple junctions need not be 120° as the cross-section need not be oriented along the triple lines. (b) Two-dimensional simulation results. Triple junctions all meet at 120° angles and grain are more equiaxed, in contrast to the results seen in three-dimensional cross-section in (a).

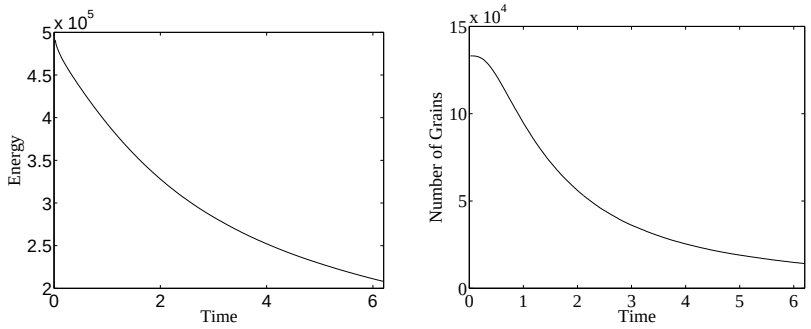

(a) (b)

Figure 5: (a) The energy $E = \sum_{i<j}(\text{area of } \Gamma_{ij})$ decreases monotonically at every iteration. (b) The number of grains N undergoes a short transition phase of slow decrease then decreases steadily from an initial value $N(0) = 133,110$ to a final value of $N(6.2021) = 14,150$.

naturally handles the topological changes involved in the disappearance of over 100,000 three-dimensional grains through $t = 6.2021$. The evolution of the number of grains is shown in Figure 5(b). After a short transition period (approximately $t = 0.4$), the number of grains in the system decreases steadily. Notice that even during this transition period, the energy of the system is decreasing quickly. The explanation for this transition period seen in the number of grains is that the initial condition is approximately Voronoi and so there are very few small grains present initially, as demonstrated in the distribution shown in Figure 7(a). The system must evolve significantly before many grains are small enough to disappear.

4.3 Grain growth rate and grain size distribution

The average grain size, $\langle R_V \rangle$, and the grain size distribution function, $f(R_V/\langle R_V \rangle)$, are probably the most important statistical quantities used to characterize an isotropic polycrystalline material. Texture distributions are also of primary importance for anisotropic polycrystalline materials, but texture is not considered in this model. Here, $R_V = (3V/4\pi)^{1/3}$ where V is the volume of a grain. Analytical approaches [12, 18, 26], experimental results (as reported in [2]), and simulation results, e.g. [2, 43], suggest that the average grain radius $\langle R_V \rangle$ exhibits power law growth as a function of time: $\langle R_V \rangle \approx Ct^n$, for t large. Analytically, the prediction $n = 1/2$ has been made using a variety of considerations. The experimental results reported in [2] find $1/4 \leq n \leq 1/2$. In their own simulation, [2] report that $n = 0.48 \pm 0.04$ for fits to long-time data (obtained by discarding data from the initial transition phase of the simulation). In [43], the authors show approximately linear long-time dependence of $\langle R_V \rangle^2$ on t. This simulation contains just 1000 grains initially, so the statistical precision of this measure is low. Furthermore, three-dimensional simulations via front tracking require that explicit assumptions be made on the types of topological changes that can occur.

As normal grain growth is characterized by the self-similarity of the distribution of $R_V/\langle R_V \rangle$, it follows that $\langle V \rangle \propto t^{3n}$. In Table 1, we fit $\langle V \rangle$ to the function $at^b + c$, where $c \approx \langle V_0 \rangle$ and mollifies the effect of the initial grain size distribution on the fit. The fits are quite tight, with all reliability factors $< 0.7\%$. Equating $b = 3n$, we find that our simulation predicts $0.501 \leq n \leq 0.518$ with 95% confidence. The fit of $2.260t^{1.515} + 3.496$ to $\langle V \rangle$ is plotted in Figure 6.

The grain size distribution function $f(R_V/\langle R_V \rangle)$ is defined by

$$f(\xi)d\xi = \text{Proportion of grains with normalized radius } R_V/\langle R_V \rangle \in [\xi, \xi + d\xi). \tag{6}$$

In Figure 7, we show histograms for this distribution at a variety of stages in the simulation. The distribution changes greatly throughout the evolution. The initial condition is approximately the Voronoi diagram for a

Time Interval	a	b	c	χ_1	χ_2	χ_3
$0 < t \leq 6.2021$	2.105	$1.550 \pm .004$	3.8617	3.79×10^{-3}	2.98×10^{-3}	2.29×10^{-3}
$1.0337 < t \leq 6.2021$	2.220	$1.524 \pm .003$	3.608	4.38×10^{-3}	2.28×10^{-3}	2.18×10^{-3}
$2.0674 < t \leq 6.2021$	2.260	$1.515 \pm .005$	3.496	4.86×10^{-3}	1.88×10^{-3}	1.57×10^{-3}
$3.1010 < t \leq 6.2021$	2.241	$1.517 \pm .013$	3.5144	6.05×10^{-3}	3.22×10^{-3}	2.89×10^{-3}

Table 1: Fit of the data $\langle V(t) \rangle$, taken from the specified time interval, to $at^b + c$. b is given with 95% confidence interval. The reliability factor $\chi \equiv \sum_i |x_i^{obs} - x_i^{calc}| / \sum_i |x_i^{obs}|$, where *obs* denotes the observed value and *calc* denotes the calculated value from the fitted function. χ_1 gives the reliability factor computed over the interval $0 < t \leq 6.2021$, χ_2 over the interval $1.0337 < t \leq 6.2021$, and χ_3 over the interval $2.0674 < t \leq 6.2021$.

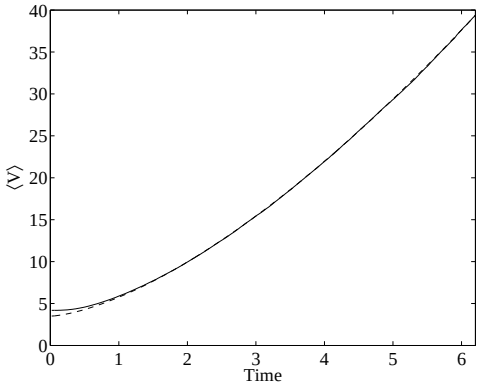

Figure 6: The average grain volume $\langle V \rangle$ compared to the best-fit power function $at^b + c$ fitted by non-linear least squares to the data from $2.0674 < t \leq 6.2021$ (see Table 1). Aside from the brief transition period, the fit is indistinguishable from the simulation results.

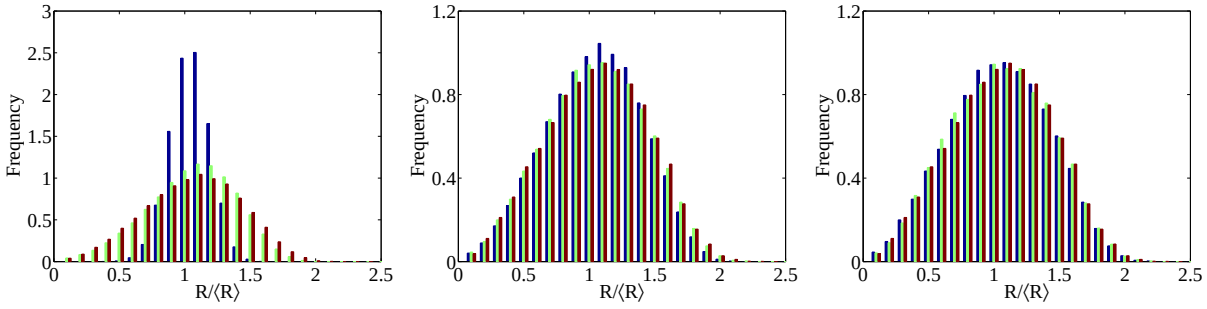

(a) (b) (c)

Figure 7: The distribution of $R_V/\langle R_V\rangle$ is shown at various times. (a) The distribution at $t = 0$ (blue), $t = 1.0337$ (green), and $t = 2.0674$ (red). The distribution is initially quite narrow but rapidly broadens. (b) At $t = 2.0674$, 4.1347, 6.2021. The distributions at $t = 4.1347$ and 6.2021 are slightly wider than at $t = 2.0674$ and exhibit self-similarity. (c) At $t = 4.1347$, 5.1684, and 6.2021, the grain size distributions appear to be self-similar, as expected in the long-term, though the number of grains in the system decreases from 24,395 to 14,150 in this timespan. Note that the scale in (a) differs from that in (b) and (c).

randomly distributed set of points. The initial distribution of grain sizes is very narrow and sharply peaked. The distribution flattens out rapidly and appears to approach a self-similar state, characteristic of normal grain growth. This self-similar distribution appears to be attained by approximately $t = 4.1347$ and is maintained thereafter, through over 10,000 grain disappearance events to the end of the simulation.

Another way to assess the self-similarity of the distribution of the grain size distribution function across iterations is to look at the evolution of the central moments of the various distributions obtained. For these distributions, the first moment is by definition 1 and the first central moment is always 0. The variance and skewness ($\mathbf{E}[(X - \mathbf{E}[X])^j]$, for $X = R_V/\langle R_V\rangle$ and $j = 2$ and 3, respectively) are plotted in Figure 8. These measures appear to be approximately constant for $t \geq 4.1347$, agreeing with the visual impression of self-similarity obtained from Figure 7(c).

Many closed-form distributions have been suggested as appropriate fits for the distribution $f(R/\langle R\rangle)$, including the Louat distribution [26], the Hillert distribution [18], the Rios distribution (a modification of the Hillert distribution) [35], the Weibull distribution (for two-dimensional grain growth) [11], and the log–normal distribution (for the distribution of grain radii in cross-sections of three-dimensional experiments) [12]. These distributions are compared to the distribution of $R_V/\langle R_V\rangle$ in Figure 9(a). The Rios distribution, with $\nu = 3.34$, appears to fit our simulation data the best. The log–normal and Louat distributions fit quite poorly, showing the wrong behavior near $R_V/\langle R_V\rangle = 0$, for large $R_V/\langle R_V\rangle$, and also peaking at $R_V/\langle R_V\rangle < 1$, all in disagreement with the simulation results. The Weibull and Hillert distributions show a better fit but can be seen both visually and by reliability factor (Table 2) to be inferior to the fit of the Rios distribution.

We also fit these distributions to data from cross-sections of the three-dimensional simulation. This is of interest as experimentally it is difficult to slice materials thinly enough for the experiments to be two-dimensional in nature, though carefully conducted thin film experiments are possible for polycrystalline grains of sufficient size. Recent progress in x-ray and and focused ion beam techniques have made measurement of grain volumes more feasible. However, it is still easiest to take cross-sections of three-dimensional grains and measure areas and effective radii in cross-section. Defining $R_A = \sqrt{A/\pi}$, where A is the area of a grain in cross-section, we generate the distribution of $R_A/\langle R_A\rangle$ from the simulation data at $t = 6.2021$. We take 512 cross-sections of constant z-value and aggregate the grain slice area data across all these cross-sections to create the simulation distribution. These cross-sections contain a total of 368,138 two-dimensional grain slices. In Figure 9(b), we fit this distribution to the closed-form distributions discussed previously. None of

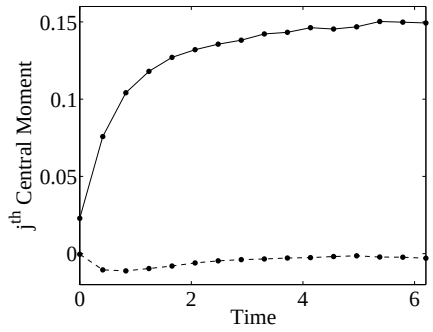

Figure 8: The variance (solid) and skewness (dashed) of the distribution of $R_V(t)/\langle R_V(t)\rangle$ are compared across iterations. While the variance of the distribution in particular changes rapidly early in the evolution, the variance and the skewness of the distribution are approximately constant for $t \geq 4.1347$, demonstrating the self-similarity of the distribution.

Grain size	log–normal			generalized Louat		Hillert	Rios		Weibull	
measure	μ	σ	χ	α	χ	χ	ν	χ	β	χ
R_A	0.074	0.574	0.335	0.685	0.152	0.389	2.14	0.221	2.07	0.171
R_V	0.056	0.417	0.282	0.741	0.330	0.128	3.34	0.031	2.80	0.104

Table 2: Least squares best-fit parameters and reliability factor χ for simulation data at $t = 6.2021$ (with 14,150 grains) to various distributions. The Rios distribution, with $\nu = 3.34$, fits the fully three-dimensional data very well. The observations made from two-dimensional cross-sections do not fit any of the distributions as well, but are best predicted by the generalized Louat distribution, with $\alpha = 0.685$. Note that the Weibull distribution does not fit the simulation distribution of $R_A/\langle R_A\rangle$ well, as the grain size distributions for two-dimensional growth and cross-sections of three-dimensional grain growth are known to disagree (for example, in [7]).

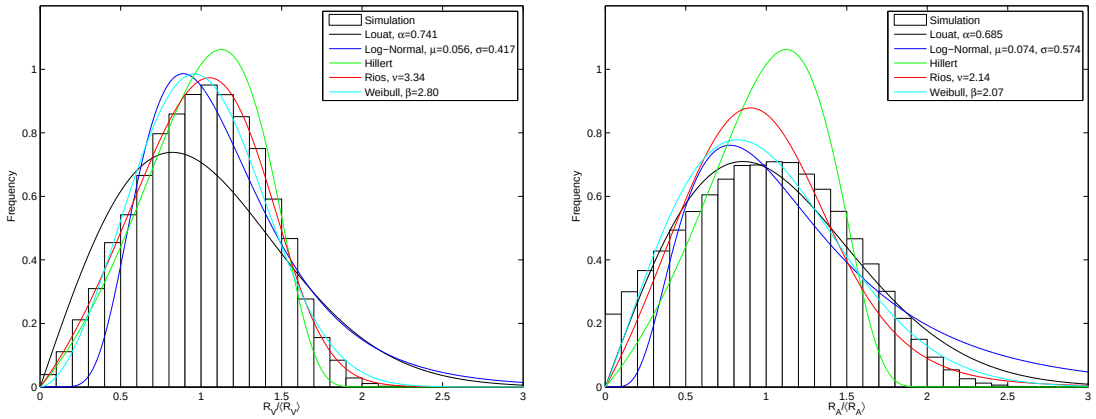

(a) (b)

Figure 9: (a) Comparison of the distribution of $R_V/\langle R_V\rangle$ at $t = 6.2021$ (with 14,150 grains) to least squares best-fit predictions to Louat, log–normal, Hillert, Rios and Weibull distributions. Note that the Louat, log–normal and Weibull distributions predict the peak of the distribution to occur at $R_V/\langle R_V\rangle < 1$, while the simulation distribution peaks to the right of 1. The peak of Hillert's distribution occurs at $R_V/\langle R_V\rangle = 9/8$, agreeing well with our simulation results. However, the Hillert's distribution predicts a higher peak and narrower distribution than we find in the normal grain growth phase. The Rios distribution is a modification of the Hillert distribution and matches the simulation results well. (b) Comparison of the distribution of $R_A/\langle R_A\rangle$ at 300 iterations (with 368,138 grains taken from the 512 cross-sections of constant z-value) to least squares best-fit predictions under the same distributions. In cross-section, the data best fits the generalized Louat distribution, though the fit is not tight. The distribution is much flatter and wider for cross-sectional data than for the full three-dimensional data.

these distributions fit the cross-sectional data as well as the Rios distribution fit the fully three-dimensional data taken from grain volumes. The Louat distribution fits the data the best with $\alpha = 0.685$ but with a reliability factor of $\chi = 0.152$. For comparison, the Rios distribution fits the three-dimensional data with $\chi = 0.031$. The distribution of $R_A/\langle R_A\rangle$ is seen in Figure 9 to be much flatter and wider than the distribution of $R_V/\langle R_V\rangle$, reemphasizing the importance of interpreting these distributions separately.

4.4 Topology

Interesting topological characteristics of the grain network include the number of faces, corners and edges of individual grains in three dimensions, and the number of edges of grains viewed in cross-section. Such characteristics have been the subject of numerous experimental studies (e.g. [5, 49, 34, 19, 50]). Here we compare the topological measures extracted from our large 3D simulation to those obtained from experimental data as well as to those from other simulations. In all the following results, we take data from $t = 6.2021$. At this time, 14,150 grains remain. In the 512 cross-sections of constant z-value, there are a total of 368,138 grain slices.

Unlike front tracking methods, methods using implicit representation of surfaces do not explicitly track topological features. The locations of these features are still well-defined: A location x is on a face, edge, or corner if for every $\varepsilon > 0$, there exist $m = 2, 3$ or 4, respectively, distinct subsets $c_1, \ldots, c_m$ and locations $x_1, \ldots, x_m$ satisfying $|x_i - x| < \varepsilon$ and $d_{c_i}(x_i) > 0$. The numerical implementation which allows association of topological descriptors to individual grains is described below. In order to count faces, corners and edges of

individual grains at any fixed time T in the evolution, each grid point in the discretization is assigned a value from the set $\{1, \ldots, N(T)\}$ corresponding to the grain at that location. The number of faces of grain i is then the number of unique identifiers different from i contained in a 1-neighborhood of the set of grid points that have identifier i. Counting corners is more challenging. In three dimensions, corners are characterized as being locations where four or more grains come together. We denote the set of all such locations as C. Because adjacent grid locations may, as part of a highly resolved corner, be marked as each being such a location, we take the number of connected components of C (as opposed to simply the number of points in C) within a single grain to be the number of corners possessed by that grain. However, this procedure will cause two corners connected by a short edge to be counted as one. To alleviate this problem, we subdivide the grid twice before applying the above procedure (so that a grid of size $n \times n \times n$ is subdivided to size $4n \times 4n \times 4n$ before counting vertices). Having thus counted the number f of faces and the number c of corners as described above, we appeal to the well-known formula $c - e + f = 2$ of Euler to infer the number e of edges of each grain. This formula holds for all polyhedra that are topologically equivalent to the sphere, which appears by inspection to be true for all the grains in our simulations of grain growth.

Data for the mean number of edges per face, mean number of faces, and mean number of corners is presented in Table 3 and compared to other simulations, to data reported for some regular polyhedrally-based grain models, and experimental results. The summary statistics vary some with the simulation technique. Ours are well within the range of values found with other simulation techniques (though the other simulations were smaller and must be less statistically valid whether due to a smaller number of grains or the potential effects of ensemble averaging). Regular polyhedra such as the pentagonal dodecahedron and the tetrakaidecahedron have been proposed as space-filling approximations for grain shapes [21, 40, 48, 29], though experimentally it is well-known that grains come in a variety of shapes and sizes. The tetrakaidecahdron matches the mean values we found well, but cannot explain more complex features of grain growth, such as the grain size distribution function (6). The Voronoi model is generated by distributing seeds uniformly at random and growing crystals simultaneously and isotropically from these seeds. The Johnson–Mehl model grows crystals isotropically but allows for varying nucleation times [29]. Both these models ignore grain boundary motion due to interface curvature, holding grain boundaries stationary once crystals meet. These are in fact models for primary recrystallization, a different annealing phenomenon occurring when cold-worked metals are annealed. The experimental data contains a wide range of values, clearly demonstrating the difficulty of computing these measures in three dimensions and also suggesting that other higher-order effects (such as variable surface tension and mobility due to grain boundary misorientation and inclination) play an important role in the evolution of polycrystalline grain systems. In future work, we will investigate extending our algorithm so that such effects can be simulated.

In Figure 10, we plot the frequency with which grains with f faces occur. The distribution is skewed towards grains with many faces. The peak occurs at $f = 12$ faces and the mean number of faces is $\langle f \rangle = 13.79$. It is natural to expect that larger grains will have more faces, on average. However, the exact nature of this relationship is unknown. Figure 11 shows the relationship between the mean value of $R_V/\langle R_V \rangle$ for grains with f faces and f, as determined from our simulation data. We also compare with measurements made by Rhines and Patterson [34] on aluminum, by Zhang, et al. [50], on α-iron, and with simulation data generated by Anderson, et al. [2], using a Potts model and kinetic Monte Carlo techniques. The fit, particularly to the data for aluminum, is quite good and appears to describe the experimental data better than the linear fit posited in [2]. The simulation results of Anderson, et al., do appear to fit the measurements of Zhang, et al., well for small f, but poorly for large f.

Stable corners occur where three triple lines come together on the surface of a grain. Under the assumption that every corner is stable, $3c = 2e$. Together with Euler's formula, we can then calculate the number of corners and edges as a function of the number of faces f as $c(f) = 2(f - 2)$ and $e(f) = 3(f - 2)$. This prediction of a linear relationship between c and f is plotted in Figure 12(a) against the values obtained from our simulation data, suggesting acceptable accuracy in our algorithm for counting corners and that our method does produce stable corners. Note that Figure 10 illustrates that very few grains have less than 4 or more than 30 faces, so small inaccuracies in the count or the presence of only a few unstable corners will cause the small deviations from the prediction shown.

	$2\langle e\rangle/\langle f\rangle$	$\langle f\rangle$	$\langle c\rangle$	Reference
Simulation	5.12	13.79	23.52	
Potts model Monte Carlo simulation	5.14	12.85	22.19	[2]
Potts model Monte Carlo simulation	—	13.7	—	[46]
Vertex dynamics	5.01	13.8	—	[47]
Phase field simulation	5.07	13.7	23.1	[24]
Surface Evolver simulation	5.05	13.5	22.6	[44]
Pentagonal dodecahedron	5	12	20	[41]
Tetrakaidecahedron	5.143	14	24	[40, 48]
Voronoi model	5.27	15.54	27.07	[29]
Johnson–Mehl model	5.10	13.27	22.56	[29]
Austenite grains	—	12.6–13.4	—	[25]
1015 α–iron grains	—	12.1	—	[50]
30 β-brass grains	5.142	14.5	24.852	[5]
β-brass grains	4.92	11.16	—	[19]
100 Al–Sn alloy grains	5.06	12.48	21.04	[49]

Table 3: Summary of topological data for simulations, regular polyhedra, and experiments. $2\langle e\rangle/\langle f\rangle$ gives the mean number of edges per face, while $\langle f\rangle$ and $\langle c\rangle$ give the mean number of faces and corners, respectively. In [25], the authors report that $\langle f\rangle$ increases as a function of annealing time, through 50 minutes.

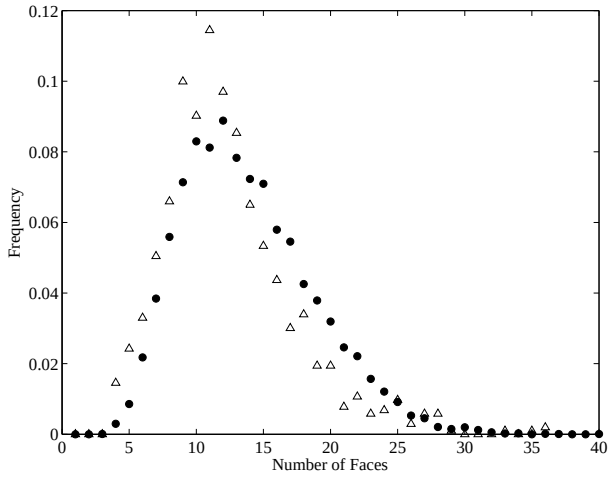

Figure 10: The proportion of grains with a given number of faces is plotted (solid circles). The peak occurs at $f = 12$ faces. Experimental data from [50] is also plotted (triangles). Note that this experimental data predicts a smaller mean number of faces (12.1) than other experimental and simulation data. See Table 3.

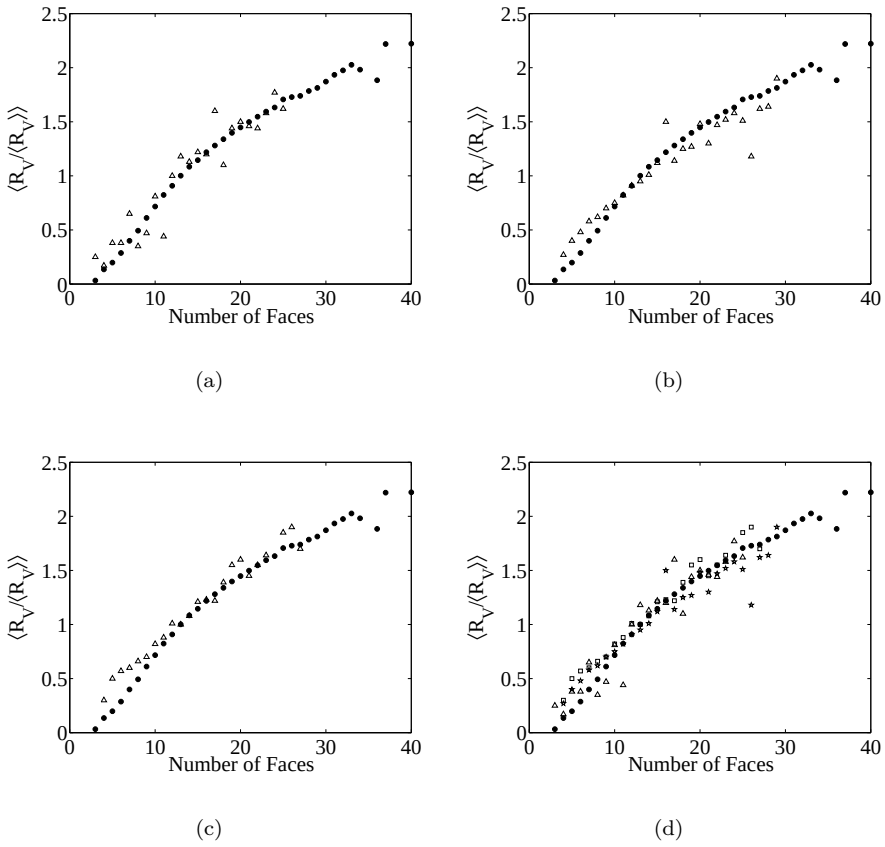

Figure 11: The relationship between the number of faces f and the mean value of $R_V/\langle R_V\rangle$ for grains with f faces is plotted (solid circles) and compared to (a) measurements for Al [34], reproduced from [2], (b) measurements reconstructed from serial sections of α-iron [50], (c) simulation data of Anderson, et al. [2]. In (d), all three are shown for comparison, with Al data marked by triangles, α-iron data by stars, and Anderson, et al. simulation data by squares.

The three-dimensional version of the Aboav–Weaire law [1, 45], proposed by Edwards and Pithia in [6] provides a relationship between the number of faces f exhibited by a grain and the mean number of faces of its neighboring grains, M_f:

$$M_f = \langle f \rangle - 1 + \frac{\langle f \rangle + \mu_f}{f}, \tag{7}$$

where μ_f is the variance of f. Following Wakai, et al., [43], we plot the mean value of $\langle fM_f \rangle$ against f and find the linear relationship predicted by Edwards and Pithia, but find the best linear fit to be $fM_f = 13.6f + 25.4$. This is in good agreement with the results of Wakai, et al., who found $fM_f = 13.3f + 23.4$. Based on their experimental data, Zhang, et al. [50] found $fM_f = 13.97f + 12.61$. Equation (7) predicts $fM_f = 12.8f + 37.7$, using the values of $\langle f \rangle$ and μ_f determined by our simulation data. Thus simulation, experiment, and theory for the three-dimensional Aboav–Weaire law agree well up to an additive constant. See Figure 12(b) for simulation data and best fit line.

In two dimensions, the well-known von Neumann–Mullins relationship [31] states that grains with more than six sides grow, and grains with fewer than six sides shrink:

$$\frac{dA}{dt} = \frac{\pi}{3}(n - 6), \tag{8}$$

where n is the number of sides of the grain. Mullins [32] proposed the following relationship for three dimensions, relating the mean growth rate of three-dimensional grains to their number of faces f:

$$\left\langle \frac{1}{R_V} \frac{dV}{dt} \right\rangle = F(f)G(f), \tag{9}$$

where

$$F(f) = \frac{\pi}{3} - 2\tan^{-1}\left(\frac{1.86\sqrt{f-1}}{f-2} \right) \tag{10}$$

and

$$G(f) = 5.35 f^{2/3} \left(\frac{f-2}{2\sqrt{f-1}} - \frac{3}{8} F(f) \right)^{-1/3}. \tag{11}$$

In Figure 12(c), we plot the simulation results for $\langle (dV/dt)/R_V \rangle$, taken from $5.9953 \leq t \leq 6.2021$. For $t = 6.0367$, 6.0780, 6.1194 and 6.1607, and $\delta t = 0.0413$ we approximate $dV/dt = (V(t+\delta t) - V(t-\delta t))/(2\delta t)$. The simulation results follow the same curve as the predictions but appear to differ by a constant additive value of approximately 2.2. Our simulation results agree well with those of Wakai, et al. [43] (using Surface Evolver, a front-tracking software package), and Weygand and Bréchet [47] (via vertex dynamics). Other generalizations have been proposed by [46] and [17]. The Weaire relationship gives a linear relationship between f and $\langle (dV/dt)/R_V \rangle$ which does not appear to fit the data presented here or in other simulations well. The Hilgenfeldt relationship agrees closely up to a scaling constant with the von Neumann–Mullins extension for 10 and greater faces and is thus not shown.

Recently, MacPherson and Srolovitz [27] published a generalization of the von Neumann–Mullins relationship to three dimensions; however the quantities involved in their formula (mean width and total edge length) are not topological in nature, unlike the two-dimensional von Neumann–Mullins relation. Furthermore, mean width is quite difficult to calculate for grains. Simplifications are known for convex polyhedra ([4]) and for regular polyhedra ([14]), but grains are irregular and may possess both convex and concave faces. We elect to compare only to the Mullins generalization, which is a topological relationship depending only on the number of faces f.

5 Summary and Conclusions

We apply the algorithm developed in [8, 7] based on diffusion generated motion of signed distance functions to a three-dimensional simulation of grain growth. This approach naturally captures the Herring condition

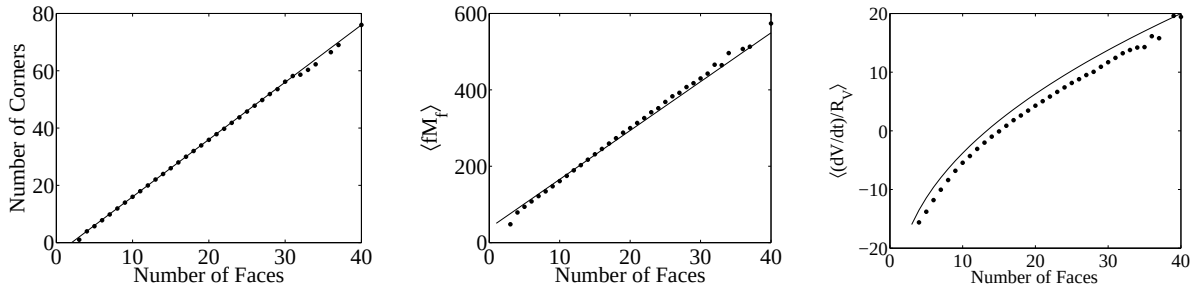

(a) (b) (c)

Figure 12: (a) There appears to be a linear relationship between the number of faces f and the mean number of corners among grains with f faces, suggesting that simulation corners are the stable meeting points of triple lines. (b) $\langle fM_f \rangle$, the mean of the product of the number of faces of a grain and the mean number of faces of its neighbors grows linearly as a function of f, matching well with the simulation results of Wakai, et al. [43]. (c) Comparison of the number of faces, f, to the mean growth rate $\langle (dV/dt)/R_V \rangle$ for grains with f faces. Simulation data from $5.9953 \leq t \leq 6.2021$ is plotted. The three-dimensional von Neumann-Mullins prediction is plotted as a solid line for comparison.

at triple junctions. In addition, numerical evidence unequivocally shows that the energy of the simulated system decays, even through topological changes. The efficiency of this algorithm allows us to compute the *accurate* evolution of over 130,000 grains until less than 15,000 grains remain. To the best of our knowledge, this evolution contained at least twice as many grains as any other currently published to date. In the next largest simulation, [42], the authors implement a phase field model initially containing 50,000 grains on a $512 \times 512 \times 512$ grid. Grains have an average initial size of approximately $14 \times 14 \times 14$ grid points, with a diffuse interface width ϵ of 3 grid points. This suggests that the initial resolution of their system is quite low. We are able to verify, with greater confidence, that the coarsening rate for normal grain growth is $\langle r \rangle \sim t^{1/2}$ and that the grain size distribution function is self-similar. We are also able to provide accurate average values of the number of edges, corners and faces of individual grains. We observe that in many cases these are in agreement with experimental results. This provides further validation that approximately normal grain growth is present in experimental settings.

Acknowledgements

This work was supported, in part, by grants from the National Science Foundation: DMS-0748333 and DMS-0810113. Selim Esedoglu was also supported by an Alfred P. Sloan Foundation fellowship.

References

[1] Aboav, D. A. The arrangement of grains in a polycrystal. *Metall. 3* (1970), 383–390.

[2] Anderson, M. P., Grest, G. S., and Srolovitz, D. J. Computer simulation of normal grain growth in three dimensions. *Philos. Mag. B 59*, 3 (1989), 293–329.

[3] Beck, P. Interface migration in recrystallization. In *Metal Interfaces*, R. Brick, Ed. American Society for Metals, Cleveland, 1952, pp. 208–247.

[4] Cahn, J. W. The significance of average mean curvature and its determination by quantitative metallography. *Trans. Am. Inst. Metall. Eng. 239* (1967), 610–616.

[5] Desch, C. H. The solidification of metals from the liquid state. *J. Inst. Metals 22*, 2 (1919), 241–276.

[6] Edwards, S. F., and Pithia, K. D. A note on the Aboav–Weaire law. *Phys. A 205* (1994), 577–584.

[7] Elsey, M., Esedoḡlu, S., and Smereka, P. Diffusion generated motion for grain growth in two and three dimensions. *J. Comp. Phys. 228*, 21 (2009), 8015–8033.

[8] Esedoḡlu, S., Ruuth, S., and Tsai, R. Diffusion generated motion using signed distance functions. *J. Comp. Phys. 229*, 4 (2010), 1017–1042.

[9] Esedoḡlu, S., and Smereka, P. A variational formulation for a level set representation of multiphase flow and area preserving curvature flow. *Commun. Math. Sci. 6*, 1 (2008), 125–148.

[10] Fan, D., and Chen, L.-Q. Computer simulation of grain growth using a continuum field model. *Acta Mater. 45*, 2 (1997), 611–622.

[11] Fayad, W., Thompson, C. V., and Frost, H. J. Steady-state grain-size distributions resulting from grain growth in two dimensions. *Scr. Mater. 40*, 10 (1999), 1199–1204.

[12] Feltham, P. Grain growth in metals. *Acta Metall. 5* (1957), 97–105.

[13] Garcke, H., Nestler, B., and Stoth, B. A multiphase field concept: Numerical simulations of moving phase boundaries and multiple junctions. *SIAM J. Appl. Math. 60*, 1 (1999), 295–315.

[14] Glicksman, M. E., Rios, P. R., and Lewis, D. J. Mean width and caliper characteristics of network polyhedra. *Philosophical Magazine 89*, 4 (2009), 389–403.

[15] Harker, D., and Parker, E. Grain shape and grain growth. *Trans. Am. Soc. Met. 34* (1945), 156–201.

[16] Herring, C. Surface tension as a motivation for sintering. In *The Physics of Powder Metallurgy*, W. Kingston, Ed. McGraw–Hill, New York, 1951, pp. 143–179.

[17] Hilgenfeldt, S., Kraynik, A. M., Koehler, S. A., and Stone, H. A. An accurate von Neumann's law for three-dimensional foams. *Phys. Rev. Lett. 86*, 12 (2001), 2685–2688.

[18] Hillert, M. On the theory of normal and abnormal grain growth. *Acta Metall. 13* (1965), 227–238.

[19] Hull, F. C. Plane section and spatial characteristics of equiaxed β-brass grains. *Mater. Sci. Technol. 4* (1988), 778–785.

[20] Kawasaki, K., Nagai, T., and Nakashime, K. Vertex models for two-dimensional grain growth. *Philos. Mag. B 60*, 3 (1989), 399–421.

[21] Kelvin, W. T. On the division of space with minimum partitional area. *Philos. Mag. 24*, 151 (1887), 503–514.

[22] Kim, S. G., Kim, D. I., Kim, W. T., and Park, Y. B. Computer simulations of two-dimensional and three-dimensional ideal grain growth. *Phys. Rev. E 74* (2006), 061605.

[23] Kinderlehrer, D., Lee, J., Livshits, I., Rollett, A., and Ta'asan, S. Mesoscale simulation of grain growth. *Mater. Sci. Forum 67–70* (2004), 1057–1062.

[24] Krill III, C. E., and Chen, L.-Q. Computer simulation of 3-D grain growth using a phase-field model. *Acta Mater. 50* (2002), 3057–3073.

[25] Liu, G., Yu, H., Song, X., and Qin, X. A new model of three-dimensional grain growth: theory and computer simulation of topology-dependency of individual grain growth rate. *Mater. Des. 22* (2001), 33–38.

[26] Louat, N. P. On the theory of normal grain growth. *Acta Metall. 22* (1974), 721–724.

[27] MacPherson, R., and Srolovitz, D. The von Neumann relation generalized to coarsening of three-dimensional microstructures. *Nature 446* (2007), 1053–1055.

[28] Mantegazza, C., Novaga, M., and Tortorelli, V. M. Motion by curvature of planar networks. *Ann. Scuola Norm. Super. Pisa–Cl. Sci. 3*, 2 (2004), 235–324.

[29] Meijering, J. L. Interface area, edge length, and number of vertices in crystal aggregates with random nucleation. *Phillips Res. Rep. 8* (1953), 270–290.

[30] Merriman, B., Bence, J. K., and Osher, S. Motion of multiple junctions: a level set approach. *J. Comput. Phys. 112*, 2 (1994), 334–363.

[31] Mullins, W. W. Two-dimensional motion of idealized grain boundaries. *J. Appl. Phys. 27*, 6 (1956), 900–904.

[32] Mullins, W. W. Estimation of the geometrical rate constant in idealized three dimensional grain growth. *Acta Metall. 37*, 11 (1989), 2979–2984.

[33] Reitich, F., and Soner, H. M. Three-phase boundary motion under constant velocities. I: The vanishing surface tension limit. *Proc. R. Soc. Edin. 126A* (1996), 837–865.

[34] Rhines, F. R., and Patterson, B. R. Effect of the degree of prior cold work on the grain volume distribution and the rate of grain growth of recrystallized aluminum. *Metall. Trans. A 13* (1982), 985–993.

[35] Rios, P. R., Dalpian, T. G., Brandão, V. S., Castro, J. A., and Oliveira, A. C. L. Comparison of analytical grain size distributions with three-dimensional computer simulations and experimental data. *Scr. Mater. 54* (2006), 1633–1637.

[36] Russo, G., and Smereka, P. A remark on computing distance functions. *J. Comput. Phys. 163* (2000), 51–67.

[37] Ruuth, S. J. A diffusion-generated approach to multiphase motion. *J. Comput. Phys. 145* (1998), 166–192.

[38] Ruuth, S. J. Efficient algorithms for diffusion-generated motion by mean curvature. *J. Comput. Phys. 144* (1998), 603–625.

[39] Smereka, P. The numerical approximation of a delta function with application to level set methods. *J. Comput. Phys 211*, 1 (2006), 77–90.

[40] Smith, C. S. Grain shapes and other metallurgical applications of topology. In *Metal Interfaces*, R. Brick, Ed. American Society for Metals, Cleveland, 1952, pp. 65–114.

[41] Smith, C. S. Some elementary principles of polycrystalline microstructure. *Met. Rev. 9*, 33 (1964), 1–48.

[42] Suwa, Y., Saito, Y., and Onodera, H. Parallel computer simulation of three-dimensional grain growth using the multi-phase-field model. *Mater. Trans. 49*, 4 (2008), 704–709.

[43] Wakai, F., Enomoto, N., and Ogawa, H. Three-dimensional microstructural evolution in ideal grain growth — general statistics. *Acta Mater. 48* (2000), 1297–1311.

[44] Wakai, F., Shinoda, Y., Ishihara, S., and Dominguez-Rodriguez, A. Topological transformation of grains in three-dimensional normal grain growth. *J. Mater. Res. 16* (2001), 2136–2142.

[45] Weaire, D. Some remarks on the arrangement of grains in a polycrystal. *Metall. 7* (1974), 157–160.

[46] Weaire, D., and Glazier, J. A. Relation between volume, number of faces and three-dimensional growth laws in coarsening cellular patterns. *Philos. Mag. Lett. 68*, 6 (1993), 363–365.

[47] Weygand, D., and Bréchet, Y. Three-dimensional grain growth: a vertex dynamics simulation. *Philos. Mag. B 79*, 5 (1999), 703–716.

[48] Williams, R. E. Space-filling polyhedron: Its relation to aggregates of soap bubbles, plant cells, and metal crystallites. *Science 161*, 3838 (1968), 276–277.

[49] Williams, W. M., and Smith, C. S. A study of grain shape in an aluminum alloy and other applications of stereoscopic microradiography. *Trans. Am. Inst. Min. Met. Eng. 194* (1952), 755–765.

[50] Zhang, C., Suzuki, A., Ishimaru, T., and Enomoto, M. Characterization of three-dimensional grain structure in polycrystalline iron by serial sectioning. *Metall. Mater. Trans. A 35A* (2004), 1927–1933.

[51] Zhao, H.-K. A fast sweeping method for Eikonal equations. *Math. Comput. 74*, 250 (2004), 603–627.

[52] Zhao, H.-K., Chan, T., Merriman, B., and Osher, S. A variational level set approach to multiphase motion. *J. Comput. Phys. 127* (1996), 179–195.